Boosting Thermoelectric Performance of Calcium Cobaltite Composites Through Structural Defect Engineering

Zongmo Shi[1,4], Can Zhang[1], Taichao Su[2], Jie Xu[1,4], Jihong Zhu[3,4], Haiyan Chen[1], Tong Gao[3,4], Mengjie Qin[1,4], Ping Zhang[1,4], Yi Zhang[1,4], Haixue Yan[4,5], and Feng Gao[1,4*]

1 State Key Laboratory of Solidification Processing, MIIT Key laboratory of Radiation Detection Materials and Devices, USI Institute of Intelligence Materials and Structure, School of Material Science and Engineering, Northwestern Polytechnical University, Xi'an, 710072, P. R. China

2 School of Materials Science and Engineering, Henan Polytechnic University, Jiaozuo, 454003, P. R. China

3 State IJR Center of Aerospace Design and Additive Manufacturing, MIIT Lab of Metal Additive Manufacturing and Innovative Design, Northwestern Polytechnical University, Xi'an, 710072, P. R. China

4 NPU-QMUL Joint Research Institute of Advanced Materials and Structure, Northwestern Polytechnical University, Xi'an, 710072, P. R. China

5 School of Engineering and Materials Science, Queen Mary University of London, London, E1 4NS, United Kingdom

Abstract: Misfit-layered $Ca_3Co_4O_9$ as a *p*-type semiconductor, is difficult to commercialize due to its relatively poor performance. Here, $Ca_{2.7-x}La_xAg_{0.3}Co_4O_9$/Ag composites prepared by spark plasma sintering were systematically investigated in terms of La^{3+} dopant levels and nano-sized Ag compacts. Multiscale microstructures of stacking fault, dislocation, and oxygen vacancy-linked defects could be recognized as an effective strategy for tuning the transport of charge carriers and phonons scattering. An increasing concentration of charge carriers was caused by the introduction of nano-sized Ag particles at the grain boundary. The multiscale structural defects served as phonon scattering centers to reduce thermal conductivity. Finally, the $Ca_{2.61}La_{0.09}Ag_{0.3}Co_4O_9$/Ag sample exhibited a maximum *ZT* of 0.35 at 1073 K. The results suggest that the interplay of structural defects provides an impetus for a huge improvement in thermoelectric performance.

Keywords: spark plasma sintering, $Ca_3Co_4O_9$, structural defects, stacking fault, grain boundary

* Corresponding author:

F. Gao, E-mail address: gaofeng@nwpu.edu.cn

1. Introduction

The growing need for renewable energy has stimulated research interests in thermoelectric generators due to their ability to generate electricity from waste heat directly and *vice versa* [1]. Thus, thermoelectric (TE) materials have received a great deal of attention and their efficiency is determined by the dimensionless figure of merit (*ZT*) of the materials, $ZT = (S^2 \cdot T)/(\rho \cdot \kappa)$, where ρ, S, κ, and T are the electrical resistivity, Seebeck coefficient, total thermal conductivity, and absolute temperature in Kelvin, respectively [2-4]. It can be seen that it is necessary to increase the transport of charge carriers and suppress thermal conductivity in order to achieve the high thermoelectric performance [5, 6].

Recently, $Ca_3Co_4O_9$ (abbreviated as CCO) has been used in a very broad and versatile range of applications, outperforming many other oxides due to its excellent oxidation resistance and low toxicity superiorities [7-9]. However, its limited thermoelectric properties may not meet the requirements in various applications. Rare earth element doping is an effective way to introduce a level of impurities and then enlarge the effective mass of the charge carrier [10-13]. Especially, the La^{3+} would be positive to reduce the phonon thermal conduction by its doping producing point defects to promote phonon scattering. Meanwhile, it is meaningful on electrical properties of CCO due to it has different electronic configurations from Ca^{2+}. Spark plasma sintering (SPS) process has received considerable attention in the fabrication of textured ceramics with high densities [14-16]. Furthermore, it may be reasonable to composite metallic silver ($\rho = 1.58 \times 10^{-3}$ mΩ·cm) due to its excellent electrical conductivity [17]. A strategy combining metallic nanoparticles with rare earth ions may be a good choice for tuning structural defects of CCO ceramics [18, 19]. In previous work, silver was introduced into the lattice of CCO and a proper amount of nano-sized Ag inclusions were added into the matrix, resulting in an increment of electrical conductivity because of the silver acting as a bridge provided a channel path for the charge carrier between grains [20-22]. Totally, it would be proposed that the multiscale structural defects originated from the doping and the composites are responsible for the high performance of thermoelectric materials.

In this paper, La^{3+} partial substitution textured composites with incorporated silver were prepared using SPS/annealing technology to optimize the thermoelectric responses. La^{3+} as the impurity level induced spin entropy fluctuation and the nano-sized Ag inclusions located at the grain boundary formed a bridge for charge carriers. The dislocation and vacancy-linked defects severely affected the transport of charge carriers. Stacking faults as phonon scattering centers could enhance phonon scattering and reduce the thermal conductivity. The maximum *ZT* value of 0.35 at 1073 K was obtained for the x= 0.09 sample due to the interplay of multiscale structural defects. It is possible to improve the thermoelectric behaviors by tuning the associativity of the structural defects.

2. Experimental procedure

Samples with different chemical compositions of $Ca_{2.7-x}La_xAg_{0.3}Co_4O_9$/10 wt% Ag ($x$= 0.03, 0.06, 0.09, and 0.12) were prepared using SPS/annealing process. The raw materials $CaCO_3$ (99.9%), Co_3O_4 (99.9%), $AgNO_3$ (99.9%), and La_2O_3 (99.7%), based on the designed stoichiometric ratios, were thoroughly ground for 12 h in the ball miller and then dried at 323 K for 8 h. After that, the mixtures were calcined at 1123 K for 10 h in a muffle furnace. Subsequently, the calcined powders were ball milled and dried again with nano-sized Ag (99.9%, average particle sizes of 30 - 50 nm) particle additives. Pellets were pressed with dimensions of Φ20 mm×4 mm under an axis pressure of 50 MPa, heated to 1173 K for 5 min using SPS equipment, and then heat-treated at 1123 K for 10 h in a tube furnace accompanied with a flow of oxygen. All the samples were polished into rectangular bars (15×4×3 mm^3) and pellets (Φ12.7×2 mm^2).

Phase compositions were identified from the powders using X-ray diffraction (XRD, Panalytical X'Pert PRO; Holland) using Cu Kα radiation over a 2θ range of 5-60 °(0.02 s/step). Scanning electron microscopy (SEM, Quanta 600 FEG; USA) was used to observe the fractured morphology and element distribution. Scanning transmission electron microscopy with a high-angle annular dark field image (HAADF-STEM, FEI Talos F200X; USA) was performed for further study, and the TEM samples were fabricated using the conventional ion-cutting method using the precision ion polishing system (PIPS, Gatan 691; USA). The

surface chemistry states were characterized by X-ray photoelectron spectroscopy (XPS, Kratos Axis Supra; Japan) using Al Kα radiation. The energy scale was calibrated by assigning 284.8 eV to the C 1s peak. The lattice dynamics were investigated through Raman scattering using a micro-Raman spectrometer (Raman, Alpha 300R; Germany). Bulk densities for the composites were measured using the Archimedes principle (ISO5018: 1983). A Hall test was carried out through a four-probe configuration with a magnetic field sweeping between ± 4 T at room temperature. The concentration (n) and Hall mobility (μ) of charge carriers were calculated from the Hall coefficient. Electrical resistivity and Seebeck coefficient were assessed between 323 K and 1073 K using a thermoelectric testing system (LSR-3/1100; LINSEIS, Germany) in a high-purity helium atmosphere. The total thermal conductivity was calculated through $\kappa=\lambda\ \rho_0\ C_p$, where λ, ρ_0, and C_p are thermal diffusion coefficient, bulk density, and specific capacity, respectively. λ and C_p were obtained using a laser flash apparatus (LFA427; NETZSCH, Germany) in an argon atmosphere. The electrical resistivity, Seebeck coefficient and power factor for the samples were parallel to the pressuring direction. Meanwhile, the thermal conductivity was perpendicular to the pressuring direction.

3. Results and discussion

Figure 1 shows the XRD patterns for the textured composites. All the obtained data were compared to the standard data (PDF#21-0139, PDF#87-0717) [23]. The main diffraction peaks corresponded well to the monoclinic $Ca_{2.7-x}La_xAg_{0.3}Co_4O_9$ phase (the space group symmetry is $C2/m$). A minor secondary phase of silver was survived. In Figure 1 (a), it is interesting to note that the (00l) peaks were found and all diffraction peaks were sharp shapes, indicating the good crystallinity of the CCO phase. The composites preferred to the obvious grain orientation along (00l) planes due to the inherent misfit-layered crystal structure and SPS process. Furthermore, the intensity characteristic peaks for the samples parallel to the pressing direction were severely weakened except for the metallic Ag peak, as shown in Figure 1 (b). The Lotgering factor (F) was evaluated from the XRD patterns within the intensity of the (00l) planes and calculated using the following equations [24, 25]:

$$F(00l) = \frac{P-P_0}{1-P_0} \quad (1)$$

$$P_0 = \frac{I_0(00l)}{\sum I_0(hkl)} \quad (2)$$

$$P = \frac{I(00l)}{\sum I(hkl)} \quad (3)$$

where $\sum I_0$ (*hkl*) and $\sum I$ (*hkl*) are the sum of intensity for the composites and the standard PDF card, respectively. **Table** 1 presents the *F* values with the increasing of the La^{3+} dopant levels. It can be seen that the textured composites could be obtained and a small fluctuation of the *F* values was observed. The *F* for the *x*= 0.09 sample reached 0.663.

To illustrate the microstructural evolution and the degree of texturing, Figure 2 shows the fractured morphology and grain orientation histogram of textured composites. The lamellar structure and a few pores of all the composites were observed. The average grain sizes reached approximately 7.5 - 9 μm. In addition, the most highly oriented polycrystalline suggested that particle agglomeration took place. **Table** 1 shows the outstanding bulk densities. The relative densities were beyond 96% for all the samples due to the aggregated arrangement of the platelet-like grains. Figure 2 (I1)-(I4) conceives that the grain orientation was an essential prerequisite for accelerating the evolution of the textured composites. Since the grain orientation and the high dense grain boundaries of the submicron-grained structure in the bulks were found, the excellent thermoelectric performance might be presented in the composites.

Figure 3 shows the backscattered electron (BSE) images and EDX mappings for the *x*= 0.09 sample. The metallic Ag inclusions and the thermoelectric phase were detected in the bulks. A part of the metallic Ag aggregated between the lamellar grains and the Ca, Co, O, Ag, and La elements homogeneously distributed, as shown in the elemental mappings (Figure 3 (c) - (h)). The schematic diagram of Ag-rich inclusions in Figure 3 (d) reveals that the survived metallic Ag was located at the grain boundaries in the matrix. It can be seen that a bridge of silver was formed and it provided the channel path for charge carriers.

TEM was performed to provide a clearly illustration into the effects of multiscale structural defects. Figure 4 shows that the nano-lamella twin crystal structures with the zone axis of (00*l*) planes, which were observed through the bright field-scanning TEM (BF-STEM) image. A nano-lamellas phase with grain sizes of 30 nm - 150 nm in the thickness exhibited an obvious *ab*-plane orientation, and the different stacking

structures were presented. Figure 4 (b) shows the detailed grain arrangements of these stacking faults. It was much different compared with the normal grain boundary. Furthermore, the dislocations regarded as linear defects would be induced between the distorted regions and the matrix, leading to a significant contribution of phonon scattering. It was interesting that the clear and clean small-angle grain boundary with the *c*-axis misorientations (about 8°) was located between the two grains. The selected area electron diffraction (SAED) and HAADF image were conducted. A SAED pattern along the [00*l*] zone axis was collected to reflect the single-crystal characteristic of the CALC, which was the monoclinic structure with the space group of *C*2/m [26]. The HAADF image provided the evidence of stacking faults. To obtain the distribution of the chemical elements, the EDX elemental mappings were implemented. This clearly demonstrated that the elements homogeneously distributed. Ag and La elements diffused into the matrix, suggesting that they were successfully introduced into the lattice. The accurate stoichiometric ratios of 16.3%, 21.7%, 57.4%, 3.1%, and 1.5% could be acquired for Ca, Co, O, Ag, and La, respectively consisting of the formula of the x= 0.09 sample.

Figure 5 shows the high-resolution transmission electron microscopy (HRTEM) images, which were employed to analyze the presence of the Ag inclusions at the grain boundary. Nano-dimension grain boundary was observed and the segmental Ag inclusions aggregated, playing a major role in improving thermoelectricity. The HAADF-STEM results showed that the lattice parameters for the matrix and the metallic Ag along the (004) and (111) planes matched well with XRD data, suggesting that no other phase was indexed in the textured composites except for the silver. The SAED of the [00*l*] zone axis are presented in Figure 5 (d) and (e), and the CALC matrix showed the multiple-crystal feature with small-angle difference among particles. Therefore, it can be seen that the Ag^{+} was introduced into the crystal lattice, and the metallic Ag was survived at the grain boundary, which was regarded as submicron scale defect. A closer inspection of the forming arrays indicated that they could scatter long-wavelength phonons together with point defect scattering through silver incorporation, which was beneficial for the reduction of lattice thermal conductivity [27-29]. Furthermore, Figure 6 presents the HRTEM with the structural defects aligned with the [00*l*] zone. In Figure 6 (a), the element deficiencies in the normal lattice showed that the oxygen vacancy-linked defects generated due to the La^{3+} entering the Ca^{2+} sites. Meanwhile, the dislocation lines

and the large distances between the atoms around the nano-grains were observed, which were attributed to the La^{3+} and Ag^{+} co-substitution. Thus, multiscale structural defects involving the stacking fault, Ag inclusions at the grain boundary, dislocation, and oxygen vacancy-linked defects were formed in the composites, which played an important role in the transport of the charge carriers and phonon scattering centers. It is readily seen that the dislocation and oxygen vacancy-linked defects were abundant nanoscale and atomic scale distortions, respectively.

Table 2 provides the electrical transport parameters for the concentration and mobility of the charge carrier at room temperature. The hole' concentration of each sample were in the order of 10^{19} cm^{-3}, suggesting that they belonged to the semiconductor. With an increase in the La^{3+} dopant levels, the hole concentration gradually decreased and then slightly increased due to the La^{3+} substitution for Ca^{2+}. The minimum hole' concentration of 4.9×10^{19} cm^{-3} was obtained for the x= 0.09 sample. It can be seen that La^{3+} and Ag^{+} ions simultaneously introducing into lattice could balance the concentration of charge carriers. Meanwhile, the inversed trend of the mobility presented, resulting in the increment of the effective mass of the charge carrier. Compared with the samples prepared using the solid-state reaction method, the concentration and mobility were largely elevated because of the high bulk density and texturing evolution in the composites.

Figure 7 (a)-(d) presents the temperature dependence of electrical resistivity, Seebeck coefficient, power factor, and the $Ln(T/\rho)$-T relationship for textured $Ca_{2.7-x}La_xAg_{0.3}Co_4O_9$/Ag composites. ρ increased firstly and then decreased with the increase in the measured temperature. It is worth noting that the metallic conduction characteristic occurred below 573 K and the metal-to-semiconductor transition for all the samples took place due to the formation of small polarons. However, the ρ of the x= 0.12 sample at room temperature reached 2.9 mΩ·cm and then decreased to 2.1 mΩ·cm at 1073 K. ρ values greatly decreased in comparison to the sample prepared with the solid-state reaction. It can clearly be inferred that there were three reasons for the decrease in electrical resistivity. Firstly, according to the compensate mechanism of the charge carrier, the substantial concentration of charge carriers was boosted due to the La^{3+} as the donor replacing the Ca^{2+}. Secondly, the bridge of the hole conduction was formed, accompanying the aggregation of metallic Ag inclusions at grain boundary, and provided the channel path of the charge carrier due to its

low work function (4.26 - 4.9 eV) [30]. Figure S1 gives the full XPS survey spectra and the resolution of the Ag 3*d* spectra. XPS provided the evidence of silver incorporation due to the XPS fitting results, and the contents of metallic Ag and lattice Ag^{+} are shown in **Table** S1. In particular, the Ag inclusions promoted hole scattering, resulting in inherently high mobility. In order to demonstrate the effect of the structural defects on hopping conduction behavior, the involved formulas can be expressed as follows [31, 32]:

$$\frac{1}{\rho} = ne\mu = \frac{nea^2A}{T} exp\left(\frac{-E_a}{k_B T}\right) \tag{4}$$

$$\ln\left(\frac{T}{\rho}\right) = \ln(C)\frac{-E_a}{k_B T} \tag{5}$$

$$O_O^x \rightarrow V_O^{\cdot\cdot} + 2e' + \frac{1}{2}O_2 \tag{6}$$

where *e*, *a*, *A*, *C*, E_a and k_B are the charge on an electron, hopping distance, pre-exponential term related to the scattering mechanism, constant, activation energy, and the Boltzmann's constant, respectively. After that, the reduction of the oxygen vacancy for the *x*= 0.09 sample was obtained from the high-resolution O 1*s* spectra (as presented in Figure S2). It showed a proper explanation for the increment in electrical conductivity, corresponding well to the oxygen vacancy-linked defects in HAADF-STEM. With the increase in the La^{3+} dopant levels, the characteristic peak for the oxygen lattice shifted to the high binding energy due to the weakly bound electrons generated to slow the excitation of O inner electrons near the substitution position. The binding energy of inner electrons was strengthened [33]. **Table** S1 presents the ratios of lattice oxygen (O_{lat}), absorbed oxygen (O_{abs}), and oxygen vacancy (O_v). Integration of these three peaks for the *x*= 0.09 sample yielded ratios of 52.0%, 30.6%, and 17.4%, respectively.

Figure 7 (b) depicts the *S* values across the whole temperature range. The *S* values were positive for all the composites, indicating the *p*-type semiconductors. It can be seen that the *S* emerged as a promising direction, firstly with the increasing La^{3+} dopant levels, before decreasing (*x* > 0.09). The *S* value of 120.5 μV/K at 1073 K was achieved for the *x*= 0.09 sample. The results of Seebeck coefficient (*S*) could be explained by the concentration and the effective mass of the charge carrier. *S* was predicted through equation [34]:

$$S = \frac{8\pi k_B^2}{3e\bar{h}^2} m_{DOS}^{*3/2} T\left(\frac{F_{1/2}(\eta)}{3n}\right)^{2/3} \tag{7}$$

where $F_{1/2}(\eta)$, $\bar{h}$, η, and $m_{DOS}^{*3/2}$ are the 1/2 order Fermi integral, Planck constant, reduced chemical

potential Fermi energy, and effective mass, respectively. It could be inferred that the enhancement of the *S* value took place with the reduction of the concentration of charge carrier and the increment of $m_{DOS}^{*3/2}$, which was positive at the La^{3+} dopant levels. According to the Heikes equation [35], the contribution of spin entropy could be used to evaluate the thermopower:

$$S = \frac{\mu_0}{eT} = -\frac{k_B}{e}\ln\left[\frac{g_3}{g_4}\left(\frac{x}{1-x}\right)\right] \quad (8)$$

where μ_0 and x are the chemical potential and the concentration of Co^{4+}, while g_3 and, g_4 are the spin-orbital degeneracies of Co^{3+} and Co^{4+}, respectively. The g_3/g_4 ratio was related to the different spin states: low-spin (LS), intermediate-spin (IS), and high-spin (HS) states of the cobalt ions [35]. Based on equation (8), the *S* was influenced by the large electronic correlations and spin entropy. The increasing *S* from spin entropy was of the order k_B/e, but it was suppressed to zero if the spin degeneracy was lifted in a magnetic field ($g_s \rightarrow 1$) [35]. This contribution of spin entropy could be enhanced with an increase in Co^{4+} degeneracy and a decrease in concentration of Co^{4+} [36]. Figure S3 (a) shows two spin-orbital doublets of the high-resolution Co 2*p* spectra. The relative Co^{3+} content ranged from 39.2% - 44.6%, as shown in **Table** S1. With the increasing of La^{3+} dopant levels, the Co^{3+} increased and confirmed that the most Co^{3+} was already in the IS state due to the transport of charge carriers depending strongly on the spin state of Co^{3+}. Figure S3 (b) shows the spin-state transition scenario, which was compatible with the electrical and thermal transport behaviors, and could clarify the observed unusual thermoelectricity response at room temperature.

The calculated power factors (*PF*s) are also included in Figure 7. Taking into account the electrical resistivity and Seebeck coefficient, the maximum *PF* value of 0.65 mW/(m·K^2) at 1073 K was obtained for the x= 0.09 sample. Figure 7 (d) shows the relationship between $Ln(T/\rho)$ and *T*. The activation energy was estimated using the Pisarenko curve, suggesting the presence of the enhancement in the transportation of the charge carrier [37].

Figure 8 shows the thermal transport properties of the $Ca_{2.7-x}La_xAg_{0.3}Co_4O_9$/Ag composites. Along with the increase in measured temperature, the total thermal conductivity (κ_{tot}) decreased from 2.22 W/(m·K) at RT to 1.82 W/(m·K) at 1073 K, which were obtained from thermal diffusivity coefficient and specific heat,

as shown in Figure S4. Temperature dependent lattice thermal conductivity (κ_l) and electronic thermal conductivity (κ_e) were calculated using the equations [38-40]:

$$\kappa_l = \kappa_{tot} - \kappa_e \quad (9)$$

$$\kappa_e = LT/\rho \quad (10)$$

where L is the Lorenz constant, taken as 2.44×10^{-8} WΩ/K^2. In Figure 8 (b), the extremely low lattice thermal conductivity could be obtained due to a wide range of multiscale structural defects that contributed to heat conduction, including vacancy-linked defects, dislocation, Ag inclusions at grain boundaries, and stacking faults. The point defect scattering gave rise to a fluctuation of the effective mass and the enhancement of the phonon-phonon scattering. Furthermore, the promising phonon transport behaviors for the reduction of thermal conductivity were also ascribed to Ag inclusions at grain boundaries and stacking faults, which originated from the anisotropic layered structure. In particular, the different scattering centers from the nano-sized Ag inclusions (NP), dislocation (D), grain boundary (B), stacking fault (SF), and point defects (PDs) in this system promoted multiscale scattering of a wide spectrum of lattice phonons [41, 42]. The κ_l of 1.75 W/(m K) for the x= 0.09 sample was about 13% lower than others at 1073 K. The κ_e values went up and down from each other because of it being a negligible parameter, suggesting that the κ_{tot} was dominated by the lattice thermal conductivity. Figure 8 (d) shows the solid lines fitted by the Debye-Callaway model, which are used to estimate the effect of the La^{3+} dopant levels on κ_l at different measured temperatures [32]. With an increase in temperature, the effect of the multiscale defects was increasingly apparent. Considering the stacking fault scatters strongly for the long- and middle-wavelength phonons, and strong vacancy-linked defects scatter for short-wavelength phonons, the lowest κ_l of 1.70 W/(m K) at 1073 K could make clear for the x= 0.12 sample.

The Raman vibration of the composites was implemented at room temperature, as shown in Figure S5. Each spectrum contained the seven Raman characteristic peaks, located at P1= 155.1 m^{-1}, P2= 176.4 m^{-1}, P3= 287.5 m^{-1}, P4= 359.3 m^{-1}, P5= 466.3 m^{-1}, P6= 539.4 m^{-1}, and P7= 615.4 m^{-1}, respectively [43]. Figure S5 (b) shows the shifting of the Raman characteristic peaks. The P1 represented the vibration of a Ca atom, and P2~P7 represented the vibration peak of an O atom. The P1 peak moved to a low wavenumber with an increase in the La^{3+} dopant levels due to the lanthanum is heavier than calcium. Meanwhile, the vibration of

the O atom occurred in the high wavenumber region. According to the harmonic vibration formula, the A_{1g} mode and E_{1g} mode associated with the Co-O stretching vibration and the planar O-O vibration was affected by oxygen vacancy-linked defects and strain effects [44].

Figure 9 (a) shows the *ZT* values calculated using the electrical and thermal transport properties for $Ca_{2.7-x}La_xAg_{0.3}Co_4O_9$/Ag composites. With the increase in the La^{3+} dopant levels, the *ZT* values for all the composites increased monotonically, which was mainly caused by the aggregation of vacancy-linked defects into arrays and the Ag inclusions at the grain boundary. The maximum *ZT* value of 0.35 for the x= 0.09 sample was obtained at 1073 K. A comparison of the independence temperature *ZT* values with previous work is shown in Figure 9 (b). It can be seen that a relatively high *ZT* was achieved in this work, which was tuned through multiscale structural defects. This result confirms that this structural defect engineering as a practicable strategy is effective for improving the thermoelectric performance of CCO bulk ceramics.

4. Conclusion

$Ca_{2.7-x}La_xAg_{0.3}Co_4O_9$/10wt% Ag ($x$= 0.03 - 0.12) composites were prepared using the SPS followed by annealing. La^{3+} partial substitution and nano-sized Ag compacts were beneficial for controlling multiscale microstructures and thermoelectric responses. The significant contributions of the structural defects were observed to clearly expound the boosted thermoelectric performance. Introducing Ag inclusions at grain boundaries formed channel paths to reduce electrical resistivity. The interplay of the vacancy-linked defects, dislocation, and stacking fault can be recognized as an effective strategy to reduce thermal conductivity. A change in the ρ value from ~ 2.4 mΩ·cm to ~ 2.1 mΩ·cm with an increase in the La^{3+} dopant levels at 1073 K was obtained. Moreover, the corresponding κ_{tot} decreased from 2.22 W/(m K) to 1.82 W/(m K) at 1073 K. The *ZT* value approached 0.35 for the x= 0.09 sample, which was 2.19 times than the pristine CCO sample. As a result, structural defect engineering has a greatly positive effect on thermoelectric performance and a new approach to CCO materials can be offered through multiscale structural defects.

Supporting Information:

Full XPS survey spectra for composites, high-resolution XPS spectra for O 1*s* and Co 2*p*, spin-state

transition scenario, temperature dependence of thermal diffusivity coefficient and specific heat, Raman results, and table of the concentration for different elements coming from XPS fitting results (PDF)

Acknowledgements

This work was supported by the National Natural Science Foundation of China (No. 51672219, 51702259), the China-Poland International Collaboration Fund of National Natural Science Foundation of China (No. 51961135301), Foundation of National High Technology Research and Development Program (No. 2015AA0172), Fundamental Research Fund for the Central Universities (No. 3102019GHJD001, 3102019MS0406), the Basic Research Program of Shenzhen (No. JCYJ20170306155944271). We would like to thank the Analytical＆Testing Center of Northwestern Polytechnical University for the measurement and discussion of XRD, STEM, and other analyses.

References

[1] He, J.; Tritt, T. M. Advances in Thermoelectric Materials Research: Looking Back and Moving Forward. Science 2017, 357, 999701-999709.

[2] Pei, Y .Z.; Wang, H.; Snyder, G. J. Band Engineering of Thermoelectric Materials. Adv. Mater. 2012, 24, 6125-6135.

[3] Chen, Z. G.; Shi, X. L.; Zhao, L. D.; Zou, J. High-Performance SnSe Thermoelectric Materials: Progress and Future Challenge. Prog. Mater. Sci. 2018, 97, 283-346.

[4] Zhao, K. P.; Qiu, P. F.; Shi, X.; Chen, L. D. Recent Advances in Liquid-Like Thermoelectric Materials. Adv. Funct. Mater. 2019, 190386701-190386719.

[5] Kim, H. S.; Liu, W. S.; Ren, Z. F. The Bridge between The Materials and Devices of Thermoelectric Power Generators. Energy Environ. Sci. 2017, 10, 69-85.

[6] Liu, W. S.; Jie, Q.; Kim, H. S.; Ren, Z. F. Current Progress and Future Challenges in Thermoelectric Power Generation: from Materials to Devices. Acta Mater. 2015, 87, 357-376.

[7] Wu, L. J.; Meng, Q. P.; Jooss, C.; Zheng, J. C.; Inada, H.; Su, D.; Li, Q.; Zhu, Y. M. Origin of Phonon Glass-Electron Crystal Behavior in Thermoelectric Layered Cobaltate. Adv. Funct. Mater. 2013, 23, 5728-5736.

[8] Thoreton, V.; Hu, Y.; Pirovano, C.; Capoen, E.; Nuns, N.; Mamede, A. S.; Dezanneau, G.; Yoo, C. Y.; Bouwmeester, H. J. M.; Vannier, R. N. Oxygen Transport Kinetics of The Misfit Layered Oxide $Ca_3Co_4O_{9+\delta}$. J. Mater. Chem. A 2014, 2, 19717-19725.

[9] Girard, S. N.; He, J. Q.; Li, C. P.; Moses, S.; Wang, G. Y.; Uher, C.; Dravid, V. P.; Kanatzidis, M. G. In Situ Nanostructure Generation and Evolution within A Bulk Thermoelectric Material to Reduce Lattice Thermal Conductivity. Nano Lett. 2010, 10, 2825-2831.

[10] Ekren, D.; Azough, F.; Gholinia, A.; Day, S. J.; Maldonado, D. H.; Kepaptsoglou, D. M.; Ramasse, Q. M.; Freer, R. Enhancing the Thermoelectric Power Factor of $Sr_{0.9}Nd_{0.1}TiO_3$ Through Control of The Nanostructure and Microstructure. J. Mater. Chem. A 2018, 6, 24928-24939.

[11] Song, X. Y.; Navia, S. A. P.; Liang, L.; Boyle, C.; Cruz, C. O. R.; Jackson, B.; Hinerman, A.; Wilt, M.; Prucz, J.; Chen, Y. Grain Boundary Phase Segregation for Dramatic Improvement of The Thermoelectric Performance of Oxide Ceramics. ACS Appl. Mater. Inter. 2018, 10, 39018-39024.

[12] Butt, S.; Xu, W.; He, W. Q.; Tan, Q.; Ren, G. K.; Lin, Y. H.; Nan, C. W. Enhancement of Thermoelectric Performance in Cd-doped $Ca_3Co_4O_9$ Via Spin Entropy, Defect Chemistry and Phonon Scattering. J. Mater. Chem. A 2014, 2, 19479-19487.

[13] Tang, J.; Xu, R.; Zhang, J.; Li, D.; Zhou, W. P.; Li, X. T.; Wang, Z. H.; Xu, F.; Tang, G. D.; Chen, G. Light Element Doping and Introducing Spin Entropy: An Effective Strategy for Enhancement of Thermoelectric Properties in BiCuSeO. ACS Appl. Mater. Inter. 2019, 11, 15543-15551.

[14] Noudem, J. G. A New Process for Lamellar Texturing of Thermoelectric $Ca_3Co_4O_9$ Oxides by Spark Plasma Sintering. J. Eur. Ceram. Soc. 2009, 29, 2659-2663.

[15] Azough, F.; Gholinia, A.; Alvarez-Ruiz, D. T.; Duran, E.; Kepaptsoglou, D. M.; Eggeman, A. S.; Ramasse, Q. M.; Freer, R. Self-Nanostructuring in $SrTiO_3$: A Novel Strategy for Enhancement of Thermoelectric Response in Oxides. ACS Appl. Mater. Inter. 2019, 11, 32833-32843.

[16] Wu, N. Y.; Holgate, T. C.; Nong, N. V.; Pryds, N.; Linderoth, S. High Temperature Thermoelectric Properties of

$Ca_3Co_4O_{9+\delta}$ by Auto-Combustion Synthesis and Spark Plasma Sintering. J. Eur. Ceram. Soc. 2014, 34, 925-931.

[17] Bittner, M.; Kanas, N.; Hinterding, R.; Steinbach, F.; Groeneveld, D.; Wemhoff, P.; Wiik, K.; Einarsrud, M. A.; Feldhoff, A. Triple-Phase Ceramic 2D Nanocomposite with Enhanced Thermoelectric Properties. J. Eur. Ceram. Soc. 2019, 39, 1237-1244.

[18] Wang, Y.; Sui, Y.; Li, F.; Xu, L. X.; Wang, X. J.; Su, W. H.; Liu, X. Y. Thermoelectrics in Misfit-Layered Oxides [(Ca, Ln)$_2$ CoO_3]$_{0.62}$[CoO_2]: from Bulk to Nano. Nano Energy 2012, 1, 456-465.

[19] Kahraman, F.; Madre, M. A.; Rasekh, S.; Salvador, C.; Bosque, P.; Torres, M. A.; Diez, J. C.; Sotelo, A. Enhancement of Mechanical and Thermoelectric Properties of $Ca_3Co_4O_9$ by Ag Addition. J. Eur. Ceram. Soc. 2015, 35, 3835-3841.

[20] Shi, Z. M.; Gao, F.; Xu, J.; Zhu, J. H.; Zhang, Y.; Gao, T.; Qin, M. J.; Reece, M.; Yan, H. X. Two-Step Processing of Thermoelectric $(Ca_{0.9}Ag_{0.1})_3Co_4O_9$/nano-sized Ag Composites with High *ZT*. J. Eur. Ceram. Soc. 2019, 39, 3088-3093.

[21] Qin, M. J.; Gao, F.; Dong, G. G.; Xu, J.; Fu, M. S.; Wang, Y.; Reece, M.; Yan, H. X. Microstructure Characterization and Thermoelectric Properties of $Sr_{0.9}La_{0.1}TiO_3$ Ceramics with Nano-sized Ag as Additive. J. Alloy. Compd. 2018, 762, 80-89.

[22] Shi. Z. M.; Xu, J.; Zhu, J. H.; Zhang, Y.; Gao, T.; Qin, M. J.; Sun, H.; Dong, G. G.; Gao, F. Effect of Platelet Template Seeds on Microstructure and Thermoelectric Properties of $Ca_3Co_4O_9$ Ceramics. Ceram. Int. 2019, 45, 1977-1983.

[23] Torres, M. A.; Costa, F. M.; Flahaut, D.; Touati, K.; Rasekh, S.; Ferreira, N. M.; Allouche, J.; Depriester, M.; Madre, M. A.; Kovalevsky, A. V.; Diez, J. C.; Sotelo, A. Significant Enhancement of the Thermoelectric Performance in $Ca_3Co_4O_9$ Thermoelectric Materials Through Combined Strontium Substitution and Hot-Pressing Process. J. Eur. Ceram. Soc. 2019, 39, 1186-1192.

[24] Xu, G. J.; Funahashi, R.; Shikano, M.; Matsubara, I.; Zhou, Y. Q. Thermoelectric Properties of Bi- and Na-Substituted $Ca_3Co_4O_9$ System. Appl. Phys. Lett. 2002, 80, 3760-3762.

[25] Noudem, J. G.; Kenfaui, D.; Chateigner, D.; Gomina, M. Toward the Enhancement of Thermoelectric Properties of Lamellar $Ca_3Co_4O_9$ by Edge-Free Spark Plasma Texturing. Scripta Mater. 2012, 66, 258-260.

[26] Asahi, R.; Sugiyama, J.; Tani, T. Electronic Structure of Misfit-Layered Calcium Cobaltite. Phys. Rev. B 2002, 66,

1551031-1551037.

[27] Wang, S.; Hui, S.; Peng, K. L.; Bailey, T. P; Zhou, X. Y.; Tang, X. F.; Uher, C. Grain Boundary Scattering Effects on Mobilities in *p*-Type Polycrystalline SnSe. J. Mater. Chem. C 2017, 5, 10191-10200.

[28] Li, W. J.; Wang, J.; Poudel, B.; Kang, H. B.; Huxtable, S.; Nozariasbmarz, A.; Saparamadu, U.; Priya, S. Filiform Metal Silver Nanoinclusions to Enhance Thermoelectric Performance of *p*-Type $Ca_3Co_4O_{9+\delta}$ Oxide. ACS Appl. Mater. Inter. 2019, 11, 42131-42138.

[29] Zhai, R. S.; Hu, L. P.; Wu, H. J.; Xu, Z. J.; Zhu, T. J.; Zhao, X.B. Enhancing Thermoelectric Performance of n-Type Hot Deformed Bismuth-Telluride-based Solid Solutions by Nonstoichiometry-Mediated Intrinsic Point Defects. ACS Appl. Mater. Inter. 2017, 9, 28577-28585.

[30] Yu, Y.; Zhang, S. Y.; Mio, A. M.; Gault, B.; Sheskin, A.; Scheu, C.; Raabe, D.; Zu, F. Q.; Wuttig, M.; Amouyal, Y.; Mirédin, O. C. Ag-Segregation to Dislocations in PbTe-based Thermoelectric Materials. ACS Appl. Mater. Inter. 2018, 10, 3609-3615.

[31] Yadav, G. G.; David, A.; Favaloro, T.; Yang, H. R.; Shakouri, A.; Caruthers, J.; Wu, Y. Synthesis and Investigation of Thermoelectric and Electrochemical Properties of Porous $Ca_9Co_{12}O_{28}$ Nanowires. J. Mater. Chem. A 2013, 1, 11901-11908.

[32] Gao, W. H.; Wang, Z. Y.; Huang, J.; Liu, Z. H. Extraordinary Thermoelectric Performance Realized in Hierarchically, Structured $AgSbSe_2$ with Ultralow Thermal Conductivity. ACS Appl. Mater. Inter. 2018, 10, 18685-18692.

[33] Wen, Y. T.; Yang, T. R.; Lee, D.; Lee, H. N.; Crumlin, E. J.; Huang, K. Temporal and Thermal Evolutions of Surface Sr-Segregation in Pristine and Atomic Layer Deposition Modified $La_{0.6}Sr_{0.4}CoO_{9+\delta}$ Epitaxial Films. J. Mater. Chem. A 2018, 47, 24378-24388.

[34] Lefevre, R.; Berthebaud, D.; Lebedev, O.; Perez, O.; Castro, C.; Gascoin, S.; Chateigner, D.; Gascoin, F. Layered Tellurides: Stacking Faults Induce Low Thermal Conductivity in The New $In_2Ge_2Te_6$ and Thermoelectric Properties of Related Compounds. J. Mater. Chem. A 2017, 5, 19406-19415.

[35] Huang, Y. N.; Zhao, B. C.; Ang, R.; Lin, S.; Huang, Z. H.; Tan, S. G.; Liu, Y.; Song, W. H.; Sun, Y. P. Enhanced Thermoelectric Performance and Room-Temperature Spin-State Transition of Co^{4+} Ions in The $Ca_3Co_{4-x}Rh_xO_9$ System. J.

Phys. Chem. C 2013, 117, 11459-11470.

[36] Zhang, D. W.; Mi, X. N.; Wang, Z. H.; Tang, G. D.; Wu, Q. S. Suppression of The Spin Entropy in Layered Cobalt Oxide $Ca_3Co_4O_{9+\delta}$ by Cu Doping. Ceram. Int. 2014, 40, 12313-12318.

[37] Wu, D.; Chen, X.; Zheng, F. S.; Du, H. C.; Jin, L.; Borkowski, R. E. D. Dislocation Evolution and Migration at Grain Boundaries in Thermoelectric SnTe. ACS Appl. Energy Mater. 2019, 2, 2392-2397.

[38] Yue, L.; Fang, T.; Zheng, S. Q.; Cui, W. L.; Wu, Y.; Chang, S. Y.; Wang, L. J.; Bai, P. P.; Zhao, H. Z. Cu/Sb Codoping for Tuning Carrier Concentration and Thermoelectric Performance of GeTe-based Alloys With Ultralow Lattice Thermal Conductivity. ACS Appl. Energy Mater. 2019, 2, 2596-2603.

[39] Sotelo, A.; Costa, F. M.; Ferreira, N. M.; Kovalevsky, A.; Ferro, M. C.; Amaral, V. S.; Amaral, J. S.; Rasekh, S.; Torres, M. A., Madre, M. A.; Diez, J. C. Tailoring $Ca_3Co_4O_9$ Microstructure and Performances Using A Transient Liquid Phase Sintering Additive. J. Eur. Ceram. Soc. 2016, 36, 1025-1032.

[40] Wang, X.; Liu, X. C.; Yan, W.; Hou, S.; Liu, X. Significant Enhancement in Seebeck Coefficient and Power Factor of $Ca_3Co_4O_9$ Thermoelectric Ceramics by SiC Addition. J. Alloy. Compd. 2019, 785, 698-705.

[41] Li, Z.; Xiao, C.; Zhu, H.; Xie, Y. Defect Chemistry for Thermoelectric Materials. J. Am. Chem. Soc. 2016, 45, 14810-14819.

[42] Ren, G. K.; Wang, S. Y.; Zhou, Z. F.; Li, X.; Yang, J.; Zhang, W. Q.; Lin, Y. H.; Yang, J. H.; Nan, C. W. Complex Electronic Structure and Compositing Effect in High Performance Thermoelectric BiCuSeO. Nat. Commun. 2019, 10, 281401-281409.

[43] An, M.; Yuan, S. K.; Wu, Y.; Zhang, Q. M.; Luo, X. G.; Chen, X. H. Raman Spectra of A Misfit Layered $Ca_3Co_4O_9$ Single Crystal. Phys. Rev. B 2007, 76, 02430501-02430505.

[44] Prasoetsopha, N.; Pinitsoontorn, S.; Bootchanont, A.; Kidkhunthod, P.; Srepusharawoot, P.; Kamwanna, T.; Amornkitbamrung, V.; Kurosaki, K.; Yamanaka, S. Local Structure of Fe in Fe-Doped Misfit-Layered Calcium Cobaltite: An X-ray Absorption Spectroscopy Study. J. Solid State Chem. 2013, 204, 257-265.

[45] Nong, N. V.; Pryds, N.; Linderoth, S.; Ohtaki, M. Enhancement of the Thermoelectric Performance of *p*-Type Layered

Oxide $Ca_3Co_4O_{9+\delta}$ Through Heavy Doping and Metallic Nanoinclusions. Adv. Mater. 2011, 23, 2484-2490.

[46] Bittner, M.; Helmich, L.; Nietschke, F.; Geppert, B.; Oeckler, O.; Feldhoff, A. Porous $Ca_3Co_4O_9$ With Enhanced Thermoelectric Properties Derived from Sol-Gel Synthesis. J. Eur. Ceram. Soc. 2017, 37, 3909-3915.

[47] Saini, S.; Yaddanapudi, H. S.; Tian, K.; Yin, Y. N.; Magginetti, D.; Tiwari, A. Terbium Ion Doping in $Ca_3Co_4O_9$: A Step towards High-Performance Thermoelectric Materials. Sci. Rep-UK 2017, 3, 4462101-4462109.

List of Tables

Table 1 Logtering factor and bulk density of the composites.

x	Logtering factor		Density/(g/cm^3)	Relative density/(%)
	perpendicular	Parallel		
0.03	0.652	0.015	5.09	96.7
0.06	0.621	0.018	5.09	96.8
0.09	0.663	0.013	5.11	97.1
0.12	0.637	0.011	5.13	97.5

Table 2 Electrical transport parameters of the composites at room temperature.

x	Carrier concentration/10^{19} cm^{-3}	Hall mobility/cm^2/(Vs)
0.03	7.8±0.31	19.2±0.27
0.06	6.4±0.26	25.8±0.15
0.09	4.9±0.08	34.7±0.36
0.12	5.7±0.12	20.7±0.21

List of Figures

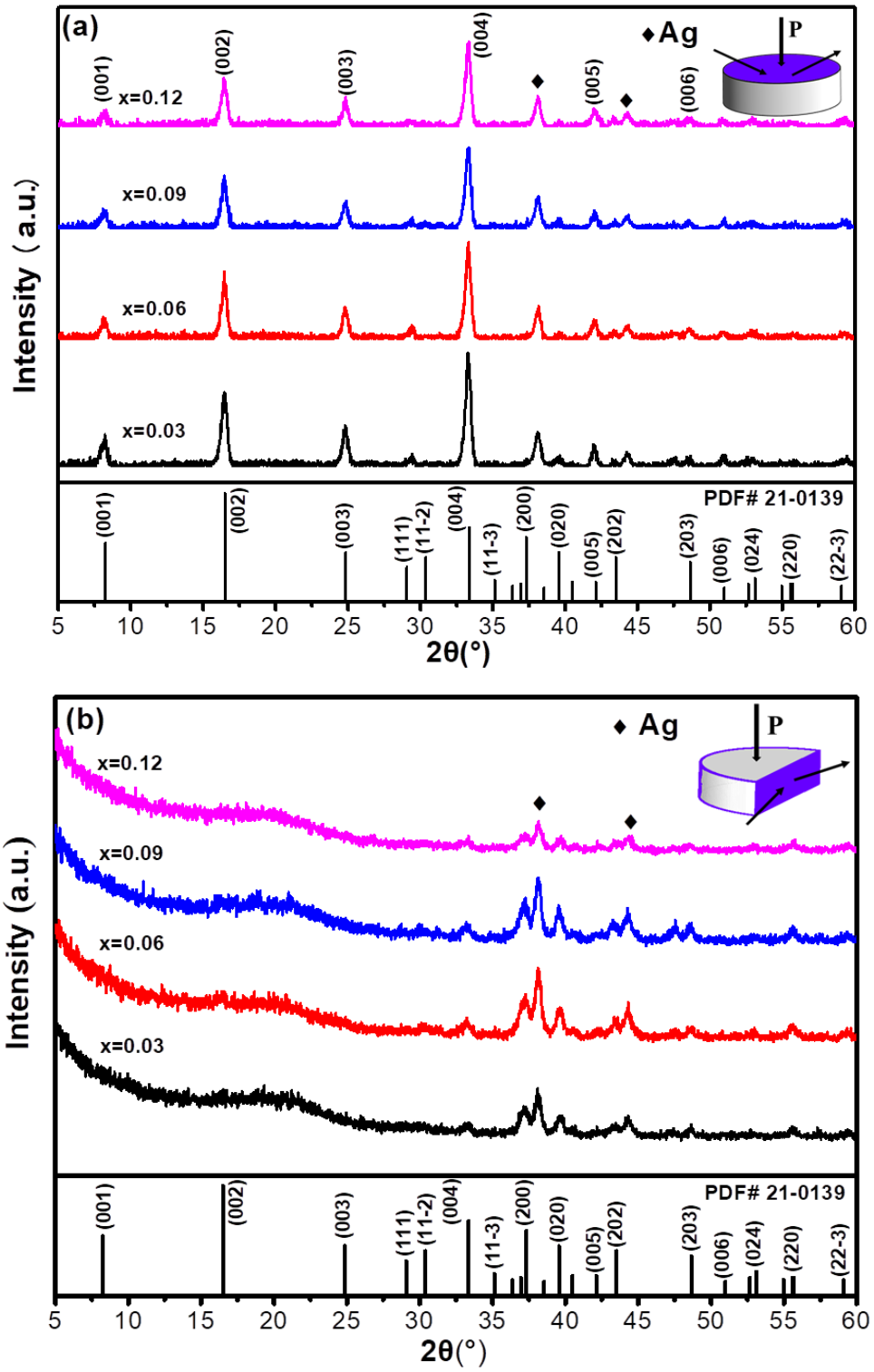

Figure 1 XRD patterns for the textured composites with the SPS/annealing process. (a) perpendicular to the pressing direction, (b) parallel to the pressing direction

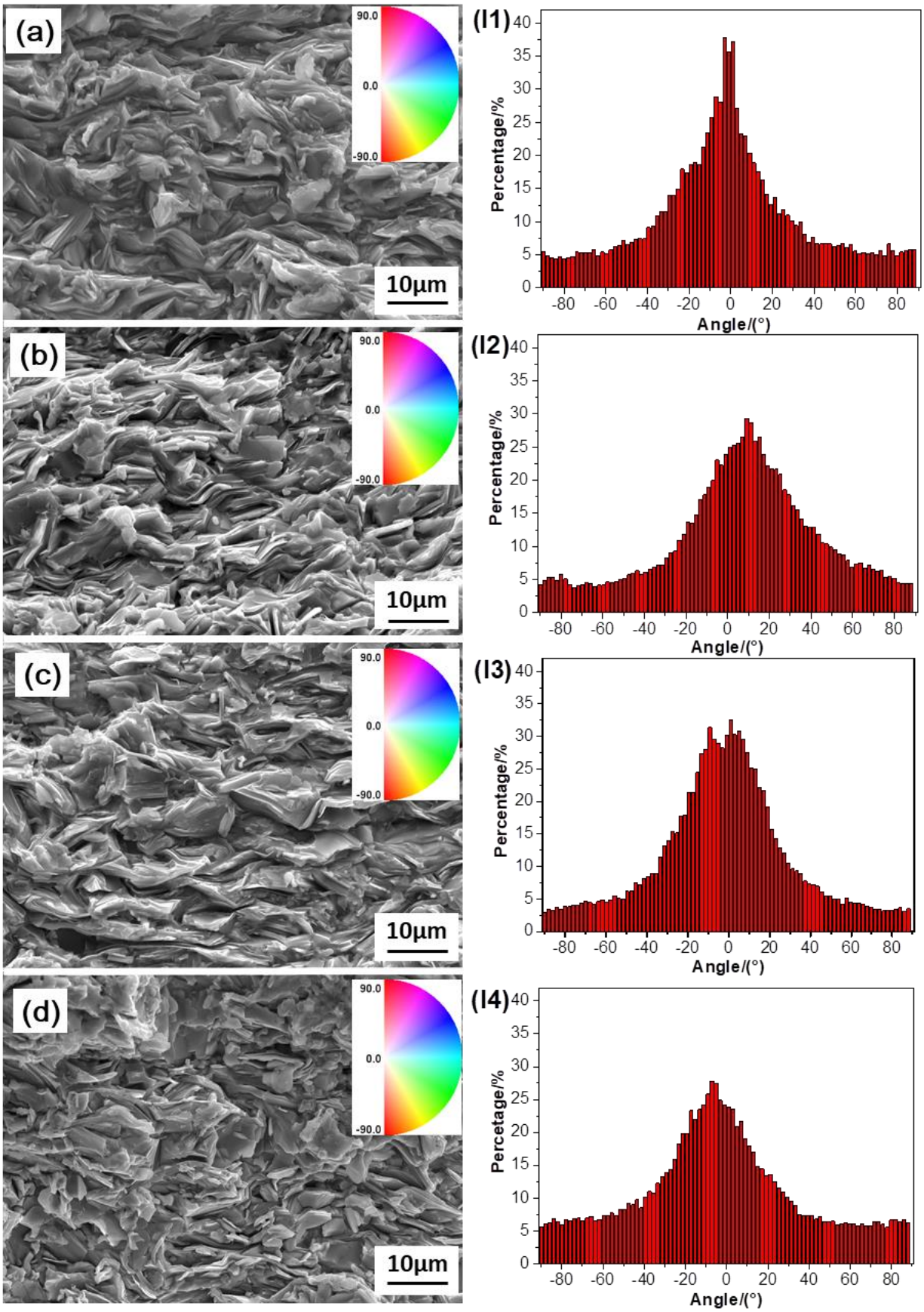

Figure 2 SEM fractured images showing the orientated morphology with the increased La^{3+} dopant levels. (a) 0.03, (b) 0.06, (c) 0.09, (d) 0.12, (I1)-(I4) the grain orientation histogram

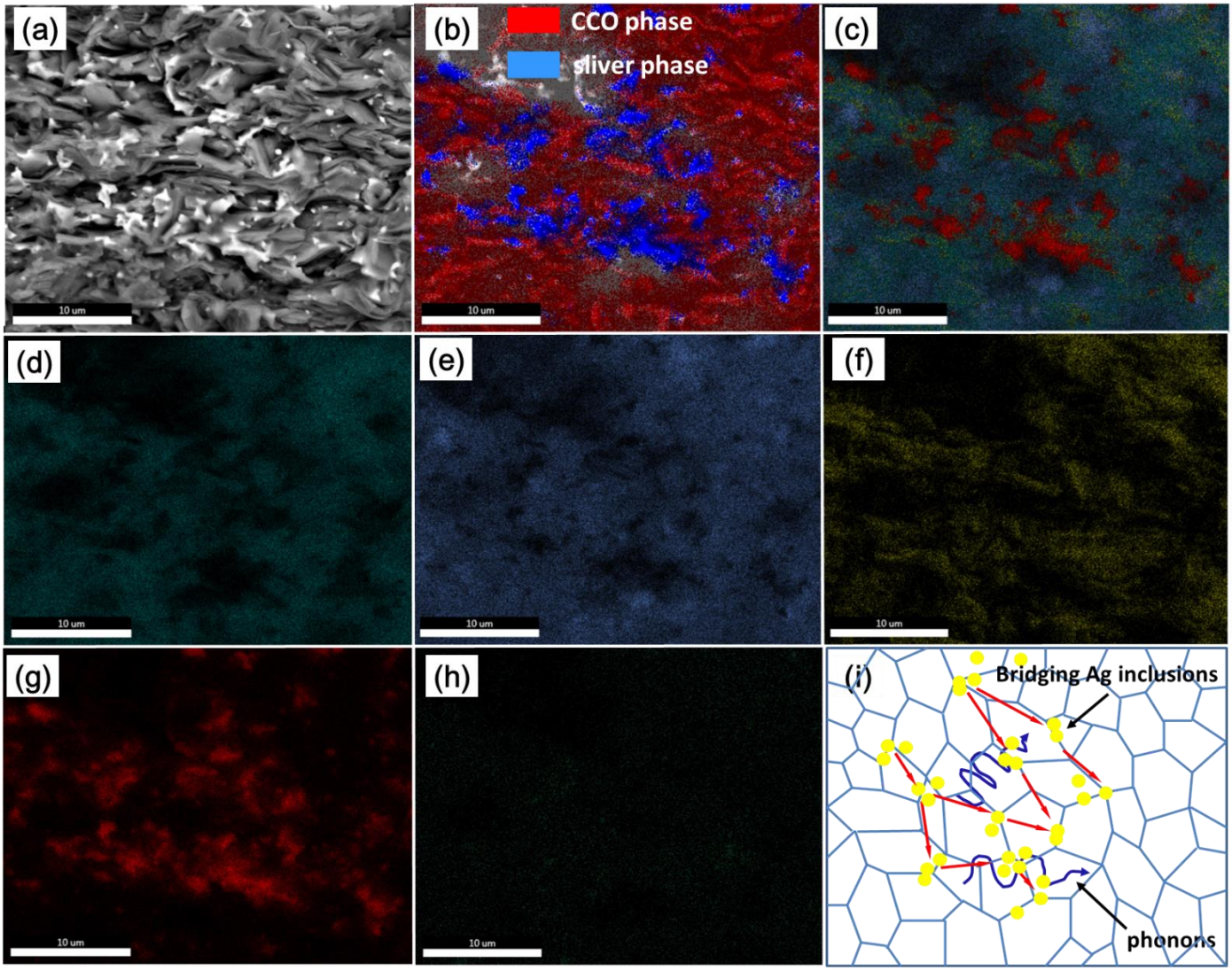

Figure 3 BSE images showing elements distribution and Ag inclusions at the grain boundary for the *x*= 0.09 composite. (a) SEM-BSE micrograph, (b) phase overlap, (c) element overlap, (d) Ca mapping, (e) Co mapping, (f) O mapping, (g) Ag mapping, (h) La mapping, (i) the sketch map of bridging Ag inclusions

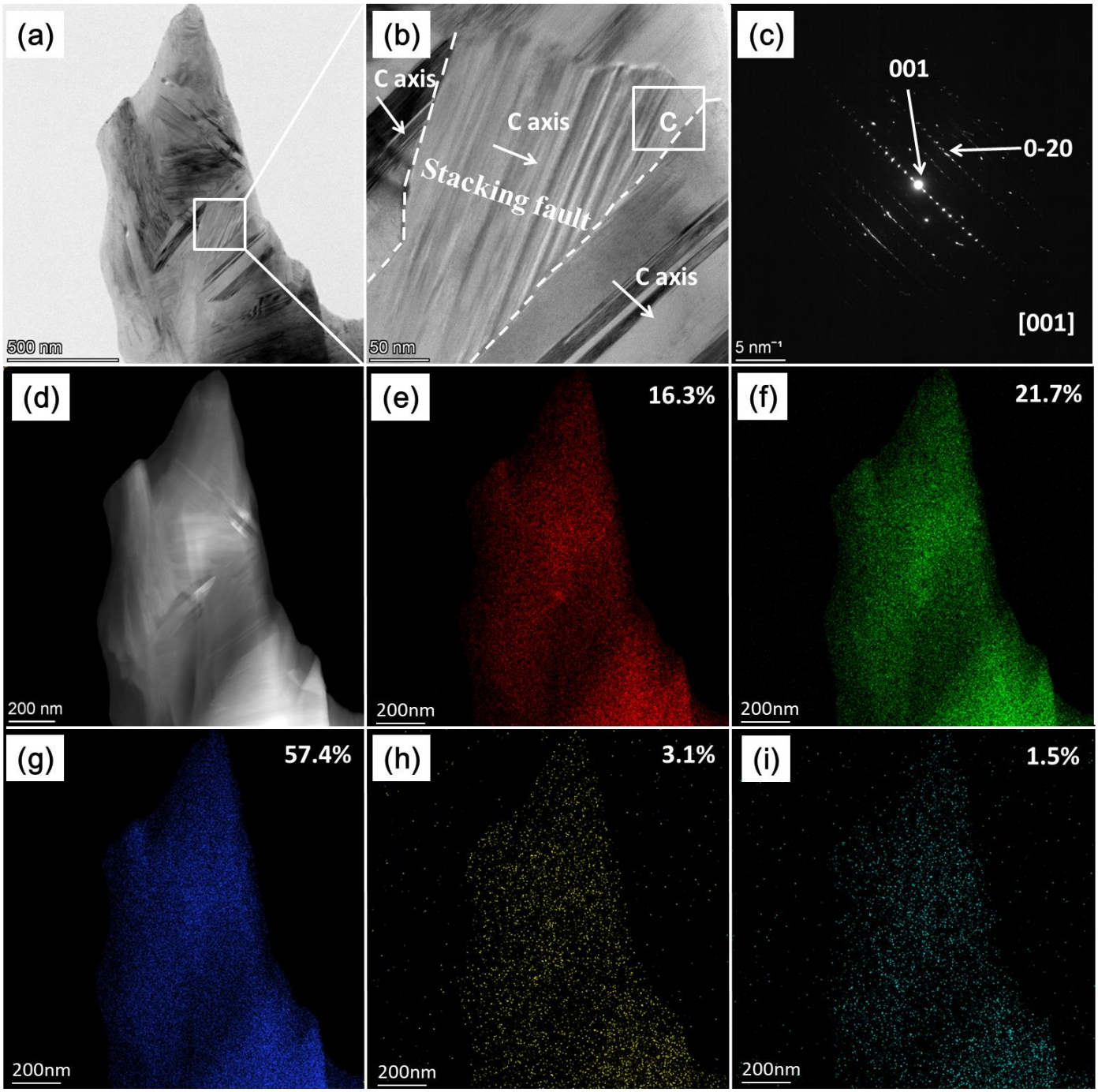

Figure 4 Low magnification TEM images taken from the *x*= 0.09 composite. (a) bright-field image, (b) nano-lamella structures, (c) SAED pattern along major zone axis, (d) HAADF image, (e) Ca mapping, (f) Co mapping, (g) O mapping, (h) Ag mapping, (i) La mapping

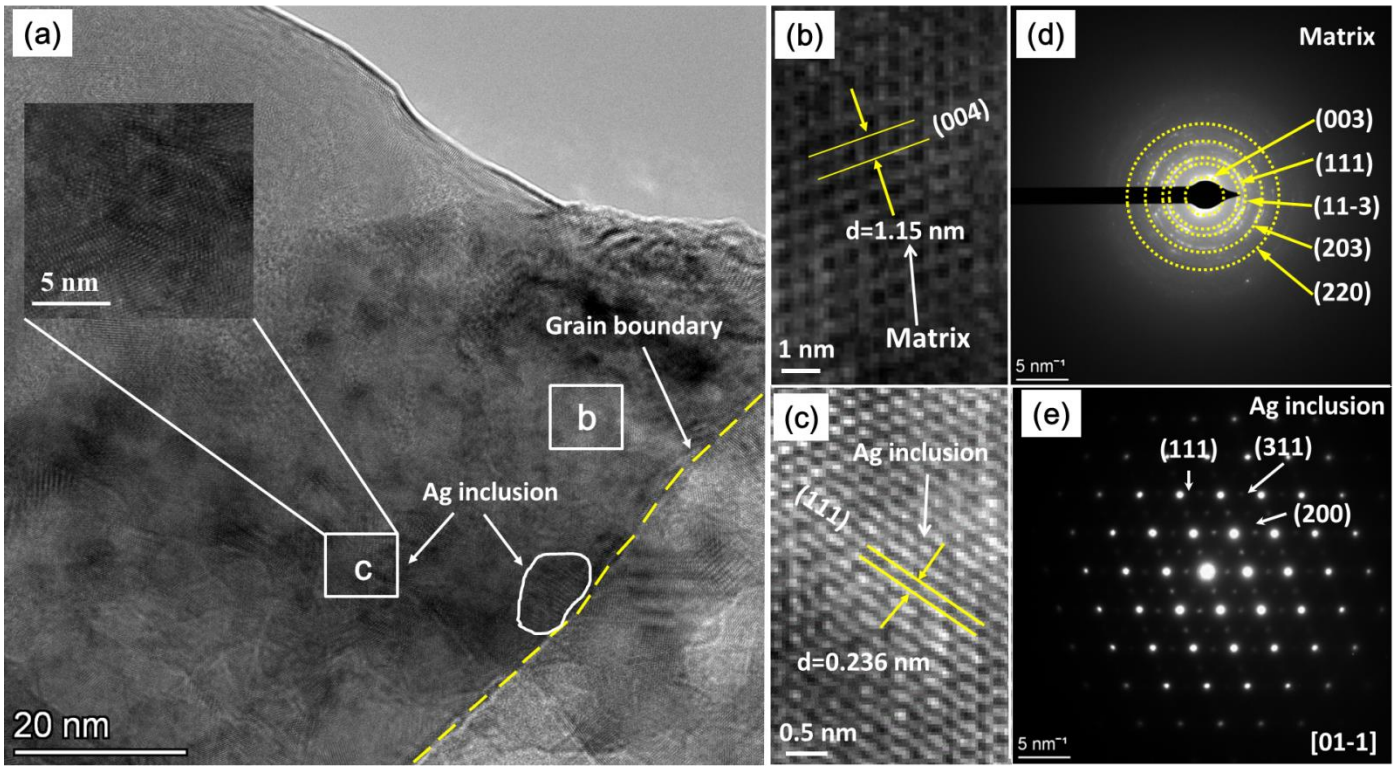

Figure 5 HRTEM images for the *x*= 0.09 composite. (a) HRTEM image with the grain boundary, (b) and (c) enlarged images from the regions in the HRTEM image, (d) and (e) SAED patterns for the matrix and Ag inclusions

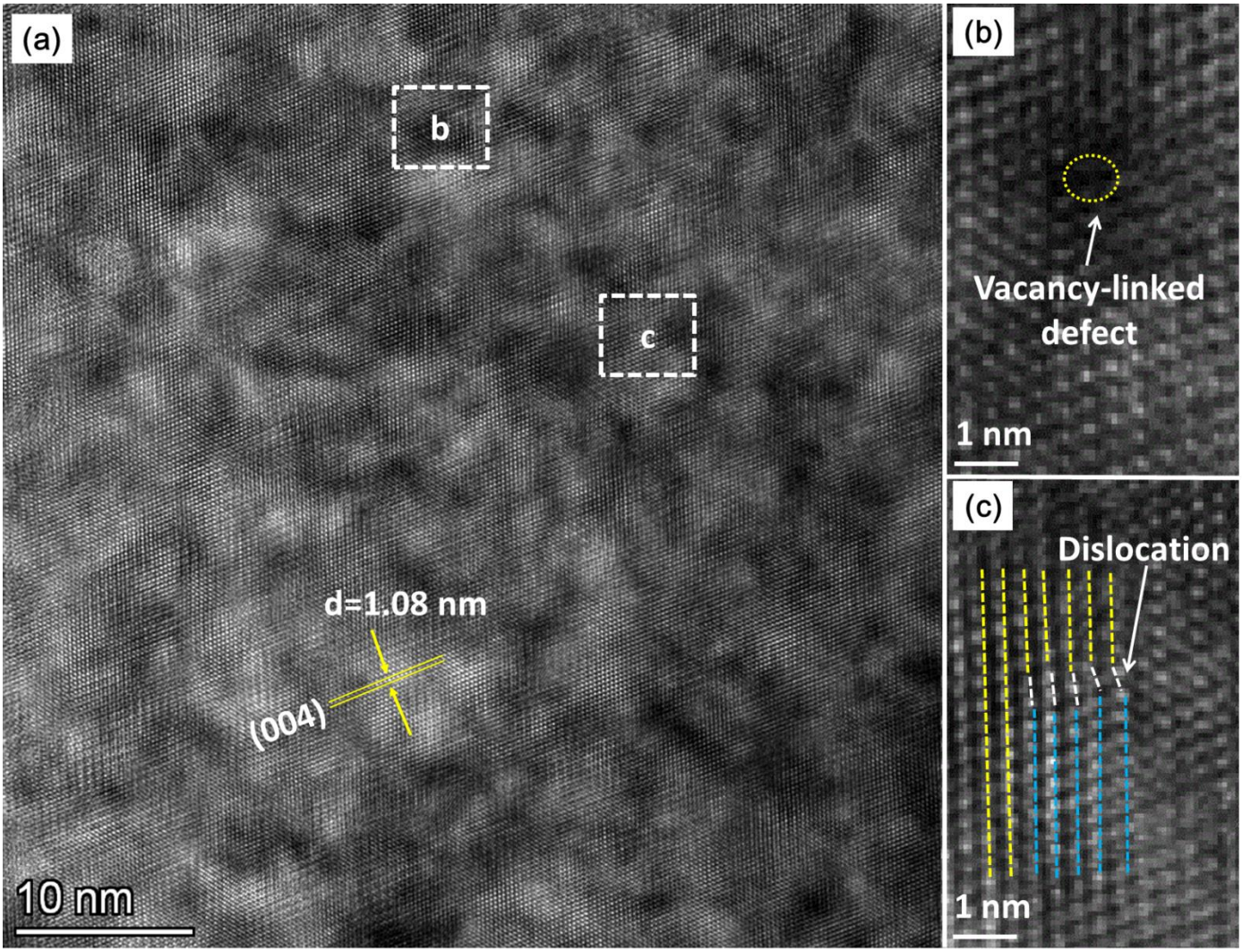

Figure 6 HRTEM images with multiscale structural defects for the *x*= 0.09 composite. (a) [001] zone axis image, (b) and (c) enlarged images from the regions in the HRTEM image showing the defects and dislocation

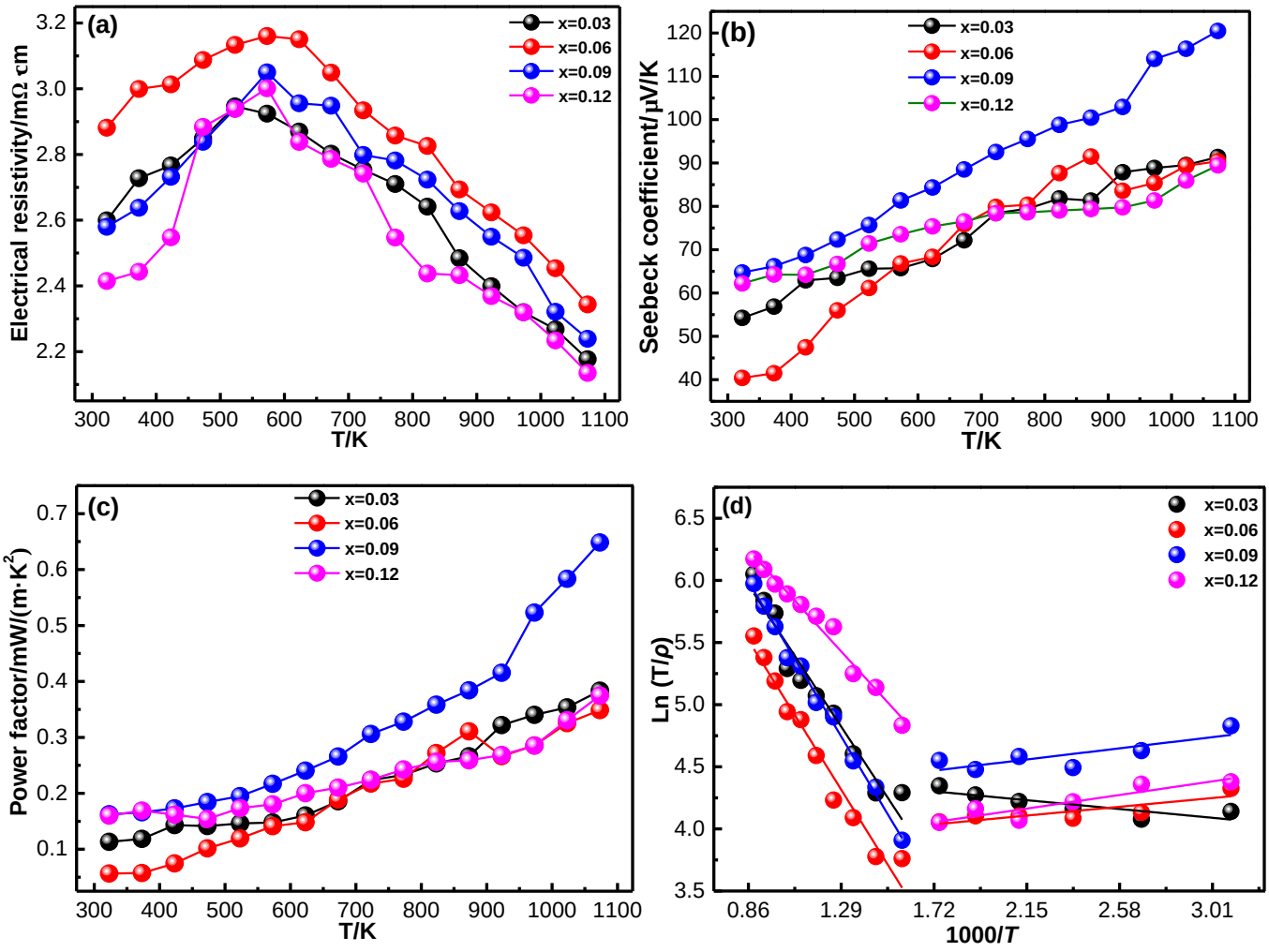

Figure 7 Temperature dependence of the electronic transport properties for $Ca_{2.7-x}La_xAg_{0.3}Co_4O_9$/Ag composites. (a) electrical resistivity, (b) Seebeck coefficient, (c) power factor, (d) $Ln(T/\rho)$-T

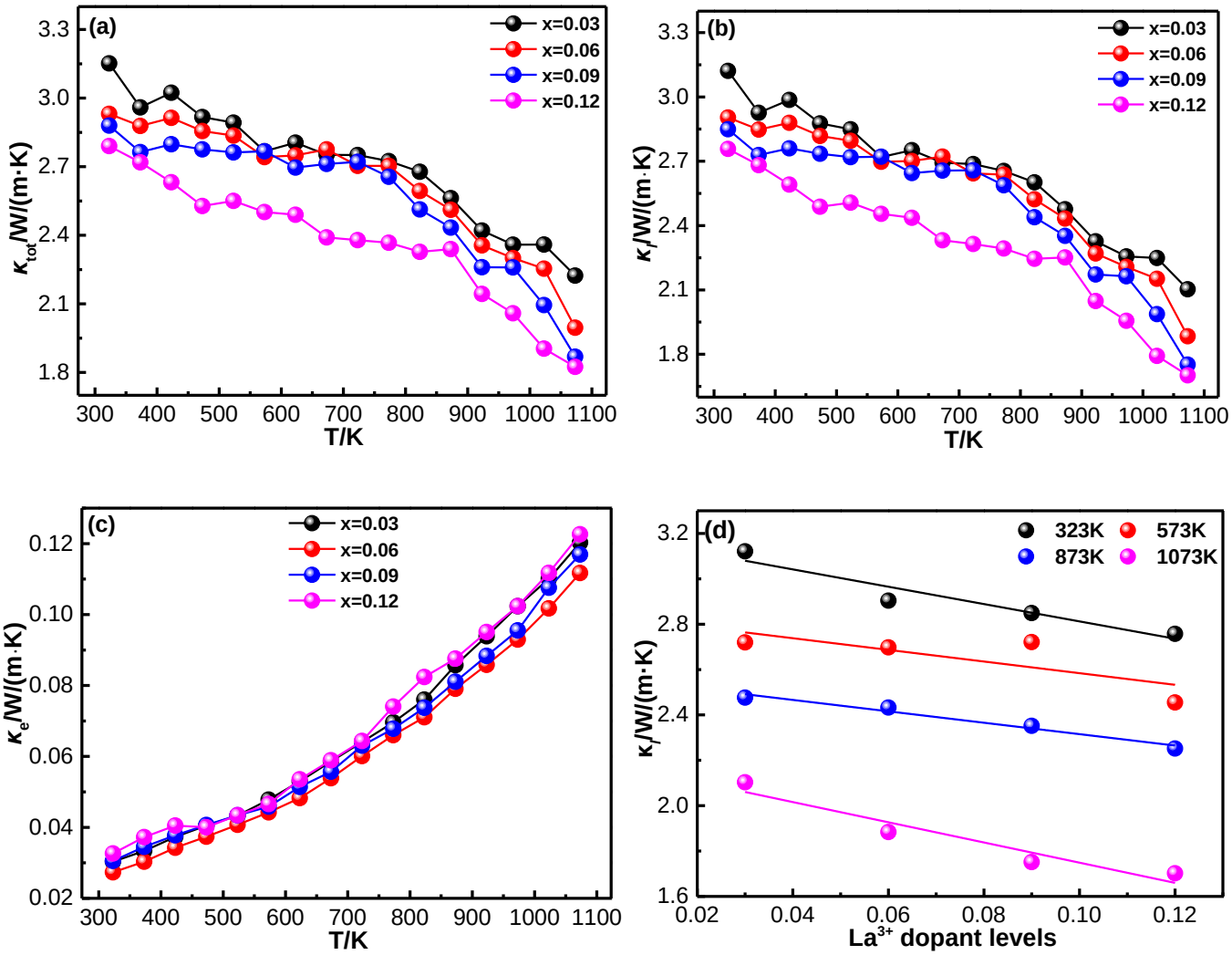

Figure 8 Temperature dependence of the thermal conductivity for $Ca_{2.7-x}La_xAg_{0.3}Co_4O_9$/Ag composites. (a) total thermal conductivity, (b) lattice thermal conductivity, (c) electronic thermal conductivity, (d) La^{3+} dopant levels dependent κ_l at different temperatures (the solid lines were estimated by the Debye-Callaway model).

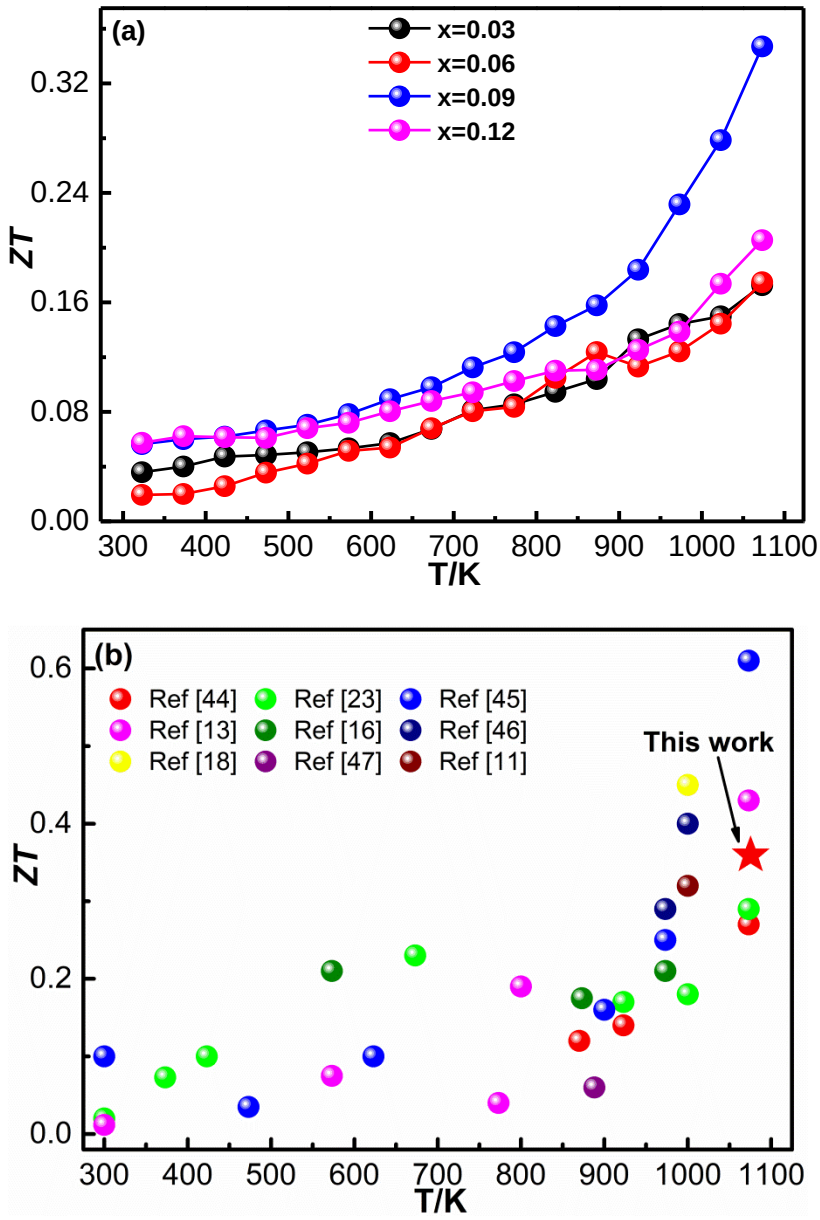

Figure 9 The *ZT* values for the CCO-based ceramics. (a) *ZT* values for the composites, (b) a comparison of previous work

Table of Contents (TOC) graphic